ACS APPLIED MATERIALS & INTERFACES

www.acsami.org

Research Article

Spoof Surface Plasmon Polariton Enabled Flexible e-Skin for Cross-Media Proximity Sensing and Material Identification

Yongze Li, Shuhao Zhang, Xuan Li, Chengkuo Lee,* Minglu Zhu,* and Tao Chen*

Cite This: *ACS Appl. Mater. Interfaces* 2026, 18, 3262−3273

Read Online

ACCESS | Metrics & More | Article Recommendations | Supporting Information

ABSTRACT: With the increasing deployment of intelligent robotics in medical rehabilitation and elderly care, sensing modalities and functionalities eventually become a critical issue in achieving comprehensive awareness regarding operational tasks. Except multidimensional tactile sensing, penetrable sensing capability with both physical and chemical sensing information can further improve operation safety and efficiency. This study presents a flexible spoof surface plasmon polariton (SSPP) sensor, fabricated by screen-printing conductive silver paste onto a thermoplastic polyurethane (TPU) substrate, which enables simultaneous contact sensing and substance identification. Operating in the 4.7−5.4 GHz frequency band, the sensor detects physical contact through time-domain phase variations, while spectral responses in the frequency domain facilitate discrimination of liquids based on their dielectric properties. The sensor exhibits remarkable mechanical robustness, with a frequency drift of less than 3% under bending and twisting deformations up to 80°, and achieves 100% classification accuracy for 12 common liquids through machine learning models. This work provides a viable pathway toward cross-media perceptual intelligence for next-generation assistive robots, supporting safe and context-aware human−robot interaction.

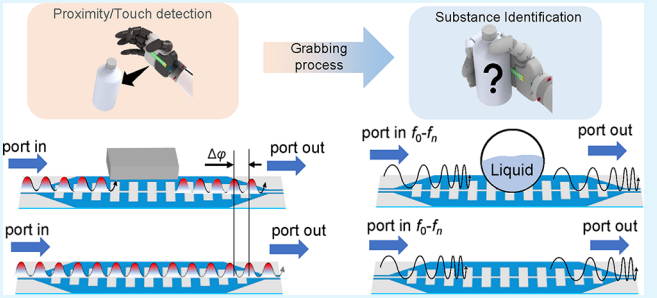

KEYWORDS: *flexible sensor, force sensing, material identification, SSPP, conformal surface plasmons*

1. INTRODUCTION

With the rapid advancement of intelligent sensing and robotics technologies, the concept of embodied intelligence has been raised. Applications of humanoid robots are progressively migrating from industrial productivity to human-centric domains, such as medical rehabilitation and elderly assistance.[1,2] In these scenarios, robots are required not only to perform physical tasks (e.g., feeding, medication delivery, and physical support) but also to possess human-like "intelligent perception" capabilities to interact with users and their surroundings in a safe, natural, and context-aware manner. The core challenge lies in achieving accurate and comprehensive perception and interpretation of the interaction status between robotic components (e.g., manipulators) and external objects, as well as discovering the internal content of the manipulated object.[3−5] For instance, in daily assistance, robots are required to conduct stable grasping via a dexterous hand with multidimensional tactile sensors, as well as to accurately identify the liquids within containers. This requirement is essential to avoiding the delivery of inappropriate substances, thereby reducing the potential risk. However, it brings a challenge regarding the integration of a compact sensing module with multimodal and cross-media sensing capabilities on robotic manipulators.[6−9]

Tactile sensors with pressure, shear force, texture, and temperature sensing functions are frequently reported by utilizing diverse mechanisms, such as piezoresistive,[10−12] capacitive,[13−15] piezoelectric,[16−18] triboelectric,[19−24] optical,[25−28] etc. A considerable number of techniques have been applied in commercial robotic manipulators, especially in dexterous hands. Tactile information-assisted complex operations can then be performed to prove the feasibility of introducing robotic services into our daily lives. However, the current sensing solutions still focus on surface information. The detection of internal content with the e-skin is rarely studied.

Radio-frequency (RF)-based sensors are showing a unique advantage in realizing penetrable detection.[29] But conventional RF structures, such as microstrip patch antennas or dipole antennas, exhibit significant resonant frequency shifts under mechanical deformations (e.g., bending or twisting), leading to instability in sensing signals.[30−33] Furthermore, as their

Received: November 5, 2025
Revised: December 24, 2025
Accepted: December 24, 2025
Published: January 5, 2026

https://doi.org/10.1021/acsami.5c20801
ACS Appl. Mater. Interfaces 2026, 18, 3262−3273

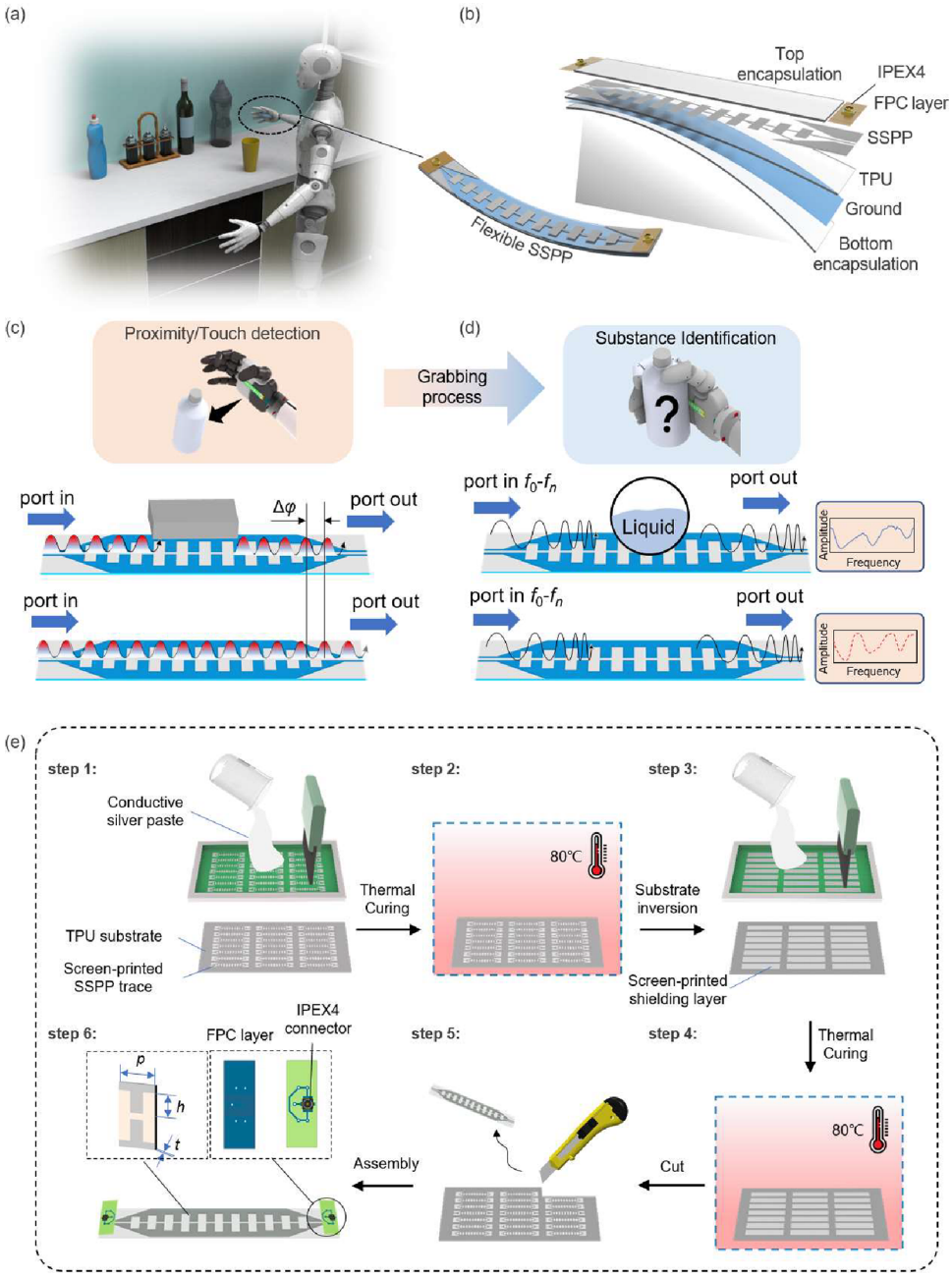

Figure 1. A flexible cross-media sensing system based on SSPP. (a) Contact sensing and liquid identification in medical and wellness care. (b) Structure of the flexible SSPP sensor. (c) Proximity/contact sensing via time-domain analysis. (d) Substance identification via frequency-domain analysis. (e) Fabrication process of SSPP sensors.

electrical length is strictly defined by the operating wavelength, the miniaturization of the device requires high-frequency operation, which brings higher requirements for microwave sources. This issue increases system complexity and overall cost, which severely limits their compatibility in the integration of robotic systems.[34−36]

To address the aforementioned challenges, flexible spoof surface plasmon polariton (SSPP) offers a groundbreaking solution.[37,38] By leveraging their unique subwavelength periodic configurations, SSPPs can tightly confine electromagnetic wave energy near the structure surface, forming subwavelength-mode field distributions.[39−42] This mechanism effectively suppresses environmental noise while enabling highly sensitive responses to external dielectric variations.[43−46] Moreover, such structures maintain stable RF performance under mechanical deformations such as bending or twisting, substantially minimizing frequency drift induced by structural strains.[47] The SSPP achieves multimodal sensing through a single planar structure.[48−50] Leveraging the propagation characteristics of conformal surface plasmons (CSPs),[51] it can be directly fabricated on or conformally attached to complex curved surfaces, enabling stable signal transmission and reliable sensing over nonplanar geometries. Specifically, for the applications in elderly assistance and dexterous robotic manipulation, flexible SSPP sensors can be conformally integrated onto robotic fingers and contact with daily objects, enabling continuous and noninvasive penetrable perception,

https://doi.org/10.1021/acsami.5c20801
ACS Appl. Mater. Interfaces 2026, 18, 3262−3273

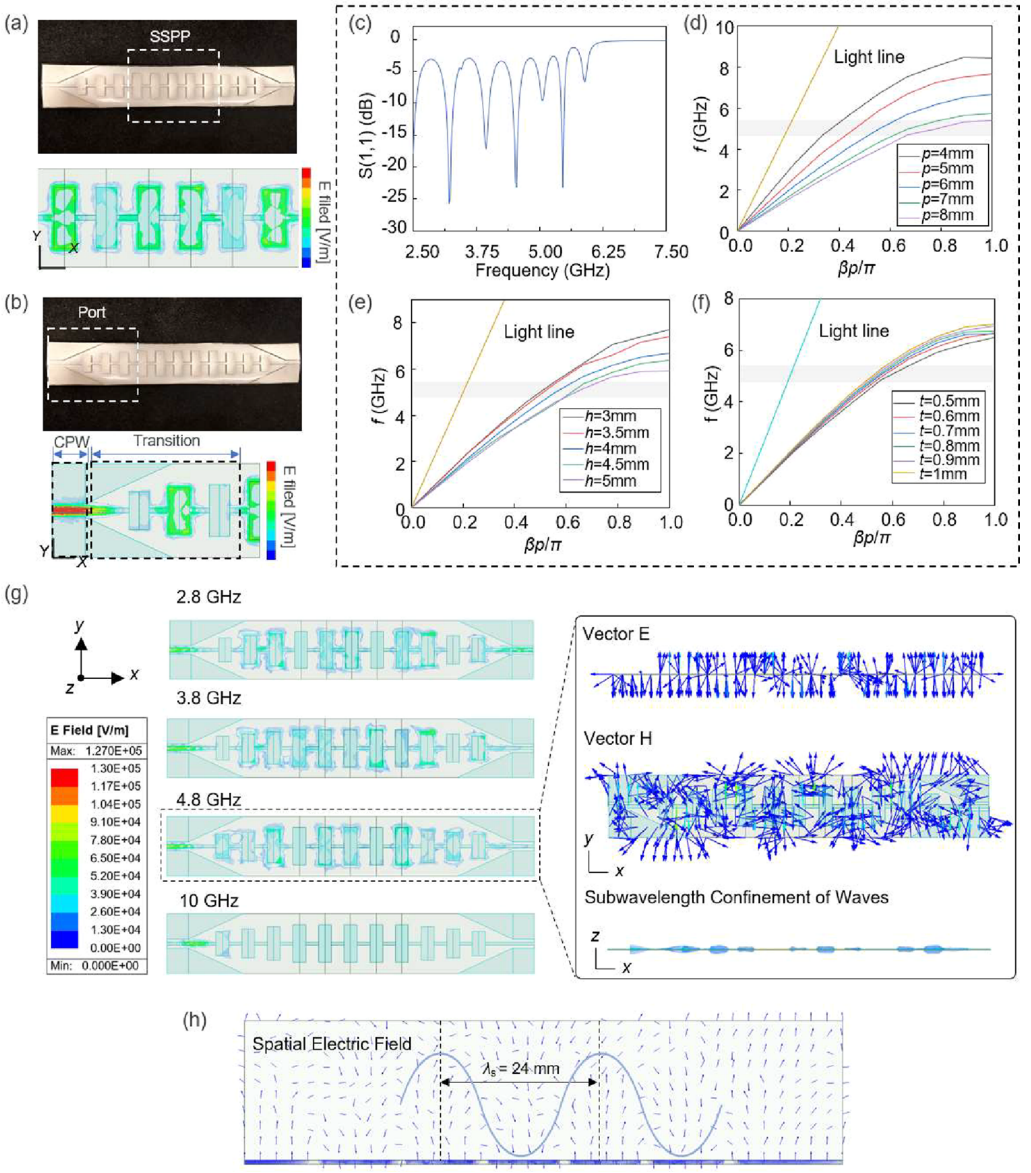

Figure 2. Design and simulation of SSPP structures. (a) Periodic structures and their simulated electric field cloud maps with p = 6 mm, h = 4 mm, and t = 0.6 mm. (b) Transmission line and transition structure of the sensor. (c) S_{11} parameters of the SSPP structure with a frequency range of 2.5− 7.5 GHz for p = 6 mm, h = 4 mm, and t = 0.6 mm. (d) Dispersion curves for varying p, with the remaining parameters as h = 4 mm. The substrate TPU had a thickness of t = 0.6 mm. The gray-shaded area shows the work frequency band. (e) Dispersion curves for varying h, with the remaining parameters as p = 6 mm and t = 0.6 mm. (f) Dispersion curves for varying t, with the remaining parameters as p = 6 mm, h = 4 mm. (g) Simulated electric field distribution of the SSPP structure at multiple frequencies. (h) Subwavelength electromagnetic wave confinement effect and spatial electromagnetic field vector distribution at 4.8 GHz.

including contact state detection and liquid property analysis (Figure 1a).

In this study, we report a flexible SSPP sensor capable of proximity sensing, physical contact detection, and the identification of liquid properties within containers. The proposed sensor was fabricated via screen printing using conductive silver paste patterned on a TPU film to form periodic SSPP structures, including a ground plane, tapered transition regions, and transmission lines. The completed flexible module was assembled with an IPEX connector attached to a flexible printed circuit (FPC). Owing to the inherent field confinement properties of the SSPP metamaterial architecture, the sensor maintains electromagnetic modal integrity under mechanical deformations, demonstrating strong immunity to frequency drift in various motions. Furthermore, the system supports multimodal and cross-media sensing functionality through the combined analysis of time-domain and frequency-domain information, which realizes contact sensing and liquid identification simultaneously. With the aid of machine learning algorithms, the demonstration of liquid identification with relatively good accuracy is presented. The results confirm that the proposed sensor is showing the feasibility of implementing multimodal and cross-media sensing by e-skin design, which can favor the application of embodied intelligence for industrial productivity and daily assistive services.

https://doi.org/10.1021/acsami.5c20801
ACS Appl. Mater. Interfaces 2026, 18, 3262−3273

2. RESULTS AND DISCUSSIONS

2.1. Design and Working Principles of SSPP

This work proposes a flexible SSPP sensor with a multilayer structure. As illustrated in Figure 1b, it consists of the following layers from top to bottom: a protective encapsulation layer, an IPEX4 connector, an FPC layer, a silver paste-based SSPP layer, a TPU substrate, a silver paste-based ground layer, and a bottom encapsulation layer. This design achieves the integration of flexible substrates and rigid cable with high-frequency signal integrity and conformability. The SSPP layer enables electromagnetic field confinement and enhanced sensitivity through its periodic subwavelength structure. The IPEX4 interface ensures low-loss transmission of high-frequency signals, and the FPC layer offers stable electrical interconnections and mechanical compliance under deformation. The TPU layer, together with the ground layer, supports microwave transmission, while the encapsulations provide mechanical protection. The ground plane isolates the SSPP structure from the influence of the mounting surface material, ensuring that microwave energy propagates only toward the sensing direction. Overall, this design allows the reliable attachment to curved surfaces of various objects while maintaining stable RF signal acquisition.

The flexible SSPP sensor achieves high-sensitivity proximity/contact detection and material identification through its multilayer metamaterial structure. In proximity/contact detection mode (Figure 1c), electromagnetic waves excite the SSPP structure through the input port, generating a highly localized field distribution along its surface. When a target object approaches or contacts the sensor surface, it alters the electromagnetic field distribution and wave propagation characteristics (phase delay). By monitoring these variations in the output signal from the port, precise proximity and contact sensing can be realized. During material identification (Figure 1d), the sensor leverages the dielectric sensitivity of the SSPP structure by performing broadband frequency sweeps ($f_0 - f_n$) to obtain the electromagnetic response spectrum (such as a resonant frequency shift and amplitude attenuation) of the liquid or other materials under test. These spectral characteristics are intrinsically linked to the physical properties of the materials, such as the dielectric constant and loss tangent. Therefore, by analyzing the phase response and amplitude-frequency characteristics of the output signal, contact detection and noninvasive classification and identification of internal materials can be achieved.

The fabrication process of the proposed flexible SSPP is illustrated in Figure 1e. The main process includes multistage screen printing and baking for preparing the ground plane, tapered transition regions, and transmission lines. One of the main advantages is the capability of massive production at a low cost. After dicing and bonding with the IPEX4 connector, the flexible SSPPs are ready for use.

2.2. Simulation and Characterization of As-Fabricated Flexible SSPP Sensor

Figure 2a presents the photo and the simulated wavelength-field distribution of the SSPP structure fabricated on a TPU substrate using conductive silver paste. The core SSPP structure comprises periodically arranged subwavelength conductive units. By tuning the geometric parameters of the unit cell, including the period (p), groove depth (h), and substrate thickness (t), the modifiable dispersion properties were achieved, enabling efficient excitation and propagation of an SSPP within a designated frequency band. This configuration significantly enhances electromagnetic field confinement and suppresses radiative loss. As illustrated in Figure 2b, the extended strip lines located at two terminals are employed as the microwave ports. The tapered transition regions beside the strip line act as a critical junction between the transmission line and the SSPP array. It is designed with a tapered profile to ensure smooth mode conversion and impedance matching. The reflection response of the SSPP structure, characterized by the S_{11} parameter across the frequency range from 2.50 to 7.50 GHz, is shown in Figure 2c. A return loss better than −20 dB is observed near specific frequencies, indicating an excellent impedance matching performance.

Figure 2d illustrates the dispersion relations of the SSPP structure under varying periods p (ranging from 4 to 8 mm), with the horizontal axis representing the normalized wave vector $\beta p/\pi$. All curves lie below the light lines of free space, confirming the subwavelength confinement characteristic of the SSPP mode. The gray shaded area indicates the operational frequency band and its corresponding dispersion properties. As the period p increases, the dispersion curves shift toward lower frequencies and exhibit increased flatness, indicating that a larger period reduces the cutoff frequency of the SSPP mode and enhances the slow-wave effect, thereby enabling strong field localization over a broader bandwidth. Figure 2e,f systematically investigates the influence of the groove depth h (varying from 3 to 5 mm) and the dielectric thickness t (varying from 0.5 to 1 mm) on the dispersion relations, respectively. In Figure 2e, increasing groove depth h causes the dispersion curves to shift toward lower frequencies with enhanced flatness, indicating that deeper grooves significantly reduce the mode cutoff frequency and strengthen the slow-wave effect. In Figure 2f, increasing the dielectric thickness t also leads to a downward shift in the dispersion curves, although this type of shift is relatively insignificant. This behavior arises because a larger dielectric thickness enhances the concentration of the electromagnetic field within the dielectric medium, thereby increasing the effective permittivity of the structure. Based on the above analysis, it can be concluded that the dielectric constant or geometric parameters (e.g., period and groove width) are the major tuning aspects for optimizing the dispersion properties, while the thickness t may serve as a minor and fine-tuning parameter.

Figure 2g visually demonstrates the spatial electromagnetic field distribution characteristics of the SSPP structure at four frequency points (2.8, 3.8, 4.8, and 10 GHz) through electric field amplitude cloud maps (maximum value: 1.27×10^5 V/m) and electromagnetic field vector distributions ($\mathbf{E}$ and $\mathbf{H}$). The electric field cloud maps show significant field enhancement and energy localization effects, with the maximum field strength concentrated in specific regions of the periodic units. By comparison with Figure 2c, it can be observed that the microwaves cannot propagate effectively along the SSPP structure at 10 GHz. The electric and magnetic field vector diagrams on the right side of Figure 2g illustrate the propagation mode and vortex formation of electromagnetic waves at 4.8 GHz. The electric field vectors are oriented along the z-axis, while the magnetic field vectors primarily form vortices in the x−y plane. According to the thickness of the as-fabricated SSPP, it is evident that microwaves are tightly confined near the periodic structure. Figure 2h illustrates the significant wavelength compression effect of the proposed

https://doi.org/10.1021/acsami.5c20801
ACS Appl. Mater. Interfaces 2026, 18, 3262−3273

SSPP structure under a 4.8 GHz excitation. The spatial electric field distribution indicates a compressed wavelength of λ_s = 24 mm, which is considerably smaller than the free-space wavelength λ_0 = 62.5 mm, yielding a compression ratio of approximately 2.6. These comprehensive results demonstrate the capability of the SSPP structure to effectively manipulate electromagnetic wave propagation and localization at the deep subwavelength scales. The design parameters of SSPP sensors are summarized in Table 1.

Table 1. Parameters of the SSPP Sensing System

parameter	value
h	4 mm
p	6 mm
t	0.6 mm
length of the SSPP	85 mm
width of SSPP	14 mm
phase amplitude	~0.2 rad
sweep frequency range	~4.78−4.89 GHz
step size	10 MHz
number of KNN training	40

The structural parameters of the SSPP sensor were designed with h = 4, p = 6, and t = 0.6 mm. Both terminals of the sensor were connected to a software-defined radio (SDR) system via IPEX4 connectors (Figure S1). As illustrated in Figure 3a, the SDR module generates a high-frequency excitation signal that is fed into the SSPP structure through the transmitting port and exciting surface waves whose propagation characteristics, such as phase, amplitude, and resonant frequency, will be modulated by the dielectric properties of the target liquid. The modulated signal is then captured by the receiving port and returned to the SDR for demodulation and analysis.

As shown in Figure 3b, the frequency-swept response of the SSPP sensor within the 4.8−5.4 GHz range exhibits three distinct peaks near 5, 5.2, and 5.4 GHz. The raw frequency-sweeping data are listed in Figure 3c. For each frequency subband, a total of 61200 complex-valued data points were collected. The averaged amplitude at each frequency point was obtained, and the standard deviation was calculated to evaluate signal stability. Owing to the TPU film substrate and the use of stretchable conductive silver paste, the sensor exhibits good mechanical flexibility. Given the increasing complexity of practical applications, the influence of structural deformation on microwave signal integrity is critical. The sensor operates in the CSP mode, whose key characteristic is that it is confined at a very deep subwavelength scale in all three spatial dimensions, enabling stability in microwave signal transmission under deformation and adaptability to morphological changes of the sensor substrate (49). We evaluated the impact of bending- and twisting-based mechanical deformation on the frequency-swept response, as shown in Figure 3d. The bending angle is denoted as α, and the twisting angle is denoted as γ.

Figure 3e presents the frequency-swept amplitude response curves of the SSPP sensor under different twisting angles (α = 20°, 40°, 60°, and 80°) across the frequency range of 4.8−5.4 GHz. The results indicate that as the twisting angle α increases, the resonant frequency exhibits only minor shifts (less than 0.02 GHz, approximately 3%) while the overall shape of the amplitude response remains highly consistent, with no observable distortion or splitting. The amplitude fluctuation across all conditions remains below 0.15. Even under the extreme twisting condition of α = 80°, the sensor maintains well-defined resonance peaks and stable in-band responses, demonstrating outstanding reliability during bending deformation. Figure 3f shows the frequency-swept amplitude characteristics of the SSPP sensor under various torsional angles (γ = 20°, 40°, 60°, and 80°) over the same frequency range. The mechanical deformation testing method for the sensor is described in Supplementary Figure S2. Additionally, we conducted reliability tests under cyclic bending deformation (Figures S3 and S4). The experimental results indicate a frequency shift of approximately 0.6% and an amplitude change of about 6% at the peak frequency (f = 5.28 GHz). The experimental results reveal that the resonant frequency remains highly stable with increasing γ, and the amplitude curves show no significant distortion. These findings confirm the outstanding electromagnetic stability of the SSPP sensor under torsional deformation. The combination of its periodic unit cell design and flexible substrate effectively suppresses electromagnetic signal drift caused by bending and twisting motions. Its electromagnetic characteristics exhibit strong immunity to variations in mechanical deformations, which are frequently encountered with robotic manipulators.

2.3. Proximity and Contact Sensing of the As-Fabricated SSPP Sensor

For proximity and contact sensing, a phase-sensitive detection system based on an SSPP sensor is illustrated through the general architecture shown in Figure 4a. This system integrates an SDR platform (GNU Radio) with a flexible SSPP sensor. The SSPP sensor enables high-precision proximity and contact detection by achieving submillimeter-level resolution in phase variation. The transmitter path employs a digital-to-analog converter (DAC) to generate a baseband signal at f_0, which is upconverted by a local oscillator (f_{RF}) and amplified through a power amplifier (PA) to excite the SSPP transducer. On the receiver side, the response signal is captured via a low-noise amplifier (LNA), downconverted, and digitized using an analog-to-digital converter (ADC). The instantaneous phase shift ($\Delta\varphi$) was extracted based on the workflow of the conjugate multiplication algorithm. Subsequently, the true and continuous absolute phase information was recovered via a phase unwrapping module. The demodulated phase output is delivered through a digital interface, enabling precise monitoring of proximity-induced electromagnetic perturbations through the SSPP sensor's near-field sensitivity.

Figure 4b displays simulated phase variations during the approach of an ethanol-filled cylindrical container toward the SSPP sensor across decreasing spacings (h_d = 1−4 mm). The corresponding electric field profiles illustrate representative confinement and distortion behaviors at key distances. The phase shift magnitude increases remarkably with reduced h_d, reaching approximately 0.2 rad at the smallest gap, showing the great distance sensitivity of the SSPP platform. Simulated field distributions verify the phase response, showing a strong spatial correlation between field enhancement and phase evolution. These results validate the proposed phase-detection mechanism as a reliable strategy for millimeter-level proximity sensing.

Figure 4c presents the phase variation response of an alcohol solution (contained in a plastic bottle) during three cyclic contact events with the SSPP sensor in practical measurements. The results indicate that the phase variation does not exhibit a monotonic increase or decrease but rather follows a

https://doi.org/10.1021/acsami.5c20801
ACS Appl. Mater. Interfaces 2026, 18, 3262−3273

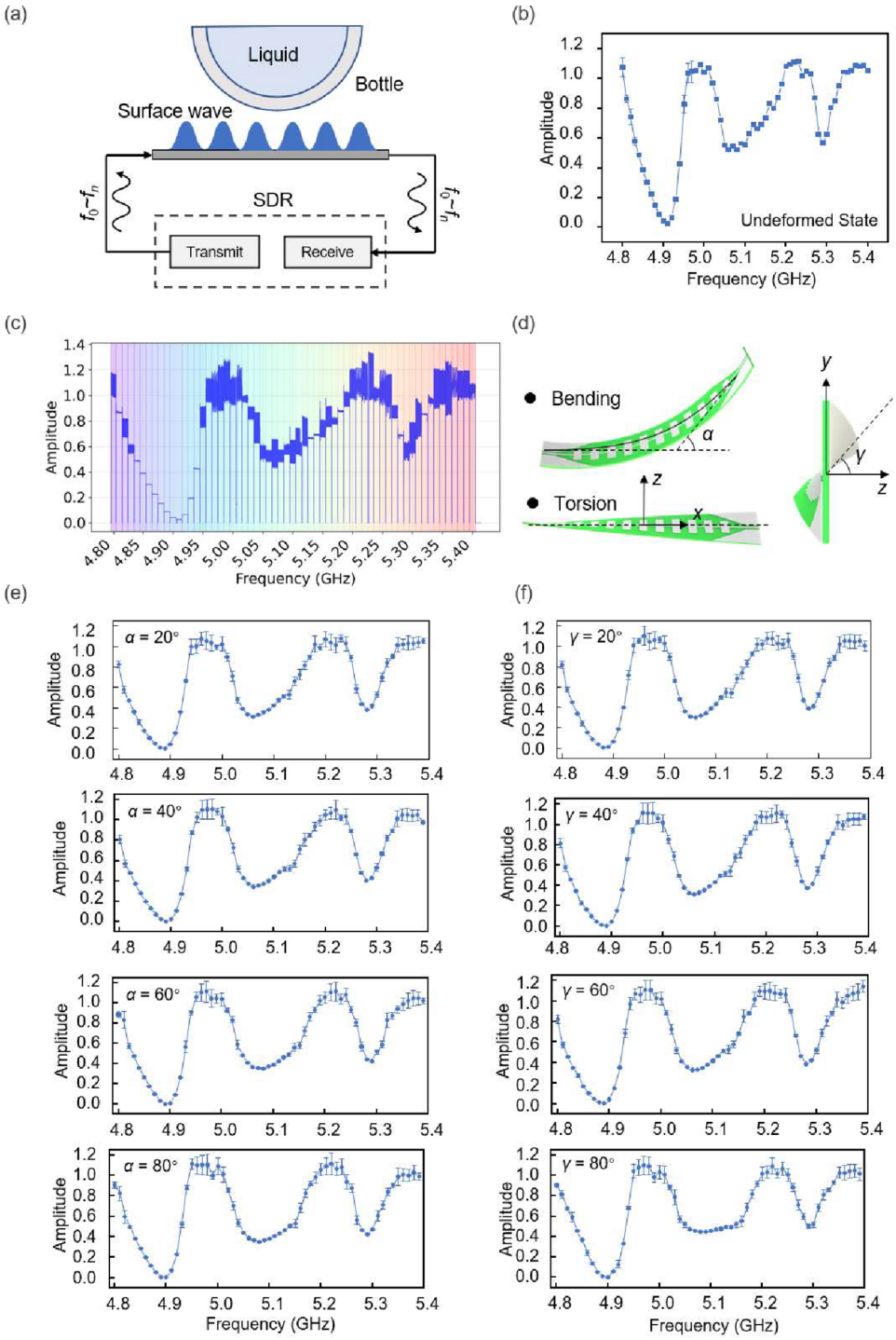

Figure 3. Sensor characteristics under mechanical deformation. (a) Schematic diagram of the SDR-based SSPP sensing system. (b) Frequency sweep data of the SSPP sensor from 4.8 to 5.4 GHz in the pristine state (without mechanical deformation. (c) Raw frequency sweep data of the SSPP sensor. (d) Schematic illustration of mechanical deformation in a flexible SSPP sensor. (e) Frequency sweep curves of the SSPP sensor under different bending angles. (f) Frequency sweep curves of the SSPP sensor under different twisting angles.

regular variation pattern. According to the enlarged data (Figure 4d), it is observed that the phase curve during the contact process comprises three distinct stages: approach, contact, and release, with the corresponding phase intervals marked by shaded gray areas. Experimental results reveal that the phase gradually increases during the approach stage. Next, it experiences an abrupt negative jump upon contact and stabilizes at a specific negative value. And then, the phase shifts to a positive value after releasing and gradually returns to the baseline. The negative phase jump and subsequent stability at the contact stage are primarily attributed to the strong electromagnetic coupling effect induced by direct contact between the alcohol solution (a high-permittivity medium) and the sensor surface. The alcohol solution significantly alters the electromagnetic field distribution on the sensor surface, enhances the fringe field coupling efficiency, and causes a resonance frequency shift and phase lag. The stabilization of the phase at a negative value reflects the concentrated

https://doi.org/10.1021/acsami.5c20801
ACS Appl. Mater. Interfaces 2026, 18, 3262−3273

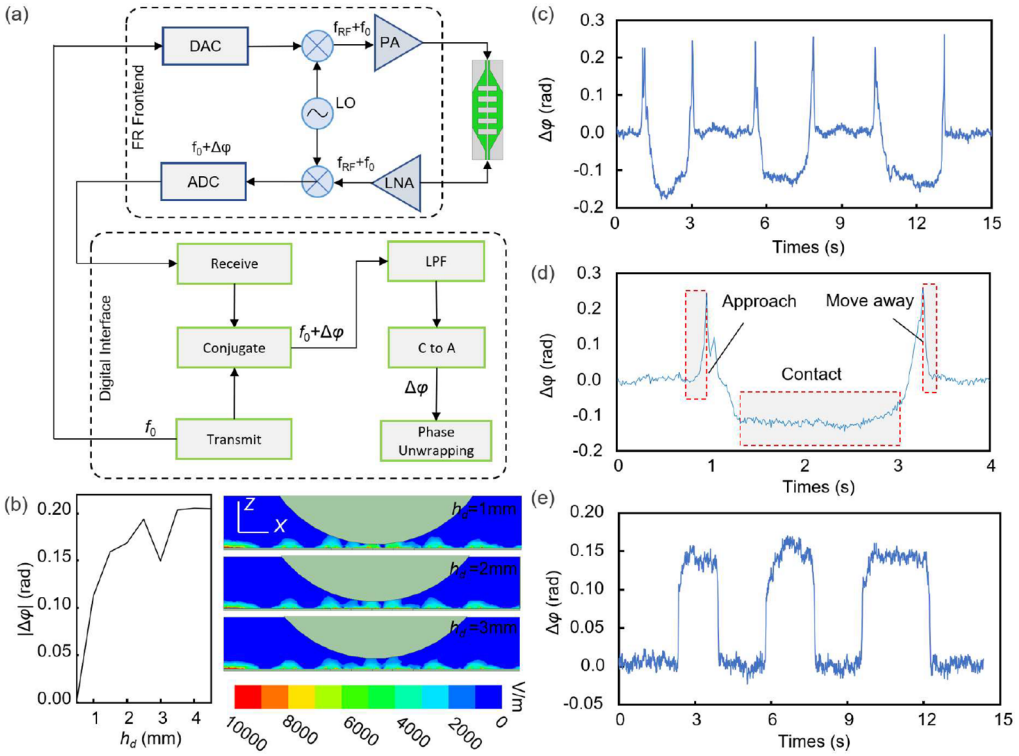

Figure 4. Proximity and contact detection capability of the flexible SSPP sensor. (a) System schematic for proximity and contact detection. (b) Simulation results of contact, where the parameters of the cylinder are set to those of the alcohol solution, and h_d denotes the distance between the cylinder and the SSPP surface. (c) Phase variation curve during three consecutive contact events with the bottle filled with alcohol. (d) Analysis of contact signal variation. Distinct phase variations occur during proximity, principal operation, and contact processes. (e) Phase variation curve during three consecutive contact events with the empty bottle.

dissipation of electromagnetic energy in the alcohol solution after contact, resulting in a stable capacitive loading effect and, thereby, producing a consistent and reproducible negative phase shift. The rise and fall of the phase curve during approach and release reflect the relative distance between the object and the sensor. This phenomenon confirms the sensitivity of the phase detection mechanism to dielectric constants as well as the status of the entire contact and release process. Moreover, the measured magnitude of the phase shift is consistent with the simulation result, both reaching $\Delta\varphi$ = 0.2.

The measured phase variation curve of an empty plastic bottle during its approach and contact with the SSPP sensor is also shown in Figure 4e. Compared with the phase response of the alcohol solution, the empty bottle exhibits a significantly smaller phase-shift amplitude ($\Delta\varphi_{max} \approx 0.15$ rad) and a gradually varying profile without the featured negative phase jump observed during the contact with the alcohol solution. This difference is primarily caused by the varied intrinsic dielectric properties: the empty plastic bottle has a much lower dielectric constant than the alcohol solution, resulting in weaker electric-field distortion during coupling with the sensor, and thus, a smaller phase variation. Meanwhile, the extremely low dielectric loss of the air inside the bottle prevents the formation of a capacitive-loading effect, which can be induced by the alcohol solution. Consequently, the contact with the empty plastic bottle only leads to a minor phase shift without a stable negative phase pattern. These distinguishable results confirm that the magnitude of phase variation is positively correlated with the dielectric constant of the medium, and that high-permittivity media can produce featured and stable phase responses upon contact through an energy-dissipation mechanism.

2.4. Material Identification of the As-Fabricated SSPP Sensor

The architecture of a material identification system based on an SDR platform, which differentiates materials through spectral response characteristics, is illustrated in Figure 5a. The transmit chain (TX) employs a Python module to generate a frequency-swept signal with carrier frequencies at $f_0 + f_n$ to excite the sensor, while the receive chain (RX) captures the response signal modulated by the materials under test and downconverts it to the baseband via a mixer. The signal processing workflow includes low-pass filtering (LPF) to remove high-frequency noise and complex-to-magnitude conversion to extract amplitude-frequency characteristics. By leveraging the distinct perturbations caused by various materials with different dielectric constants on the sensor's resonance frequency and amplitude, the system acquires characteristic spectra through frequency sweeping to achieve penetrable material identification.

In addition to substances whose dielectric constant varies little with frequency (e.g., air and oil), the permittivity of water-based materials such as water,[52] alcohol,[53] vinegar,[54] and honey[55] shows increasingly distinct differences as frequency rises within the 1−5 GHz range. Therefore, within the frequency span supported by the SDR (50 MHz−6 GHz), a higher frequency band was selected as the sweep range. The dielectric properties of each sample are summarized in Table 2. Figure 5b displays the swept-frequency amplitude responses of the SSPP sensor for 12 different materials (non-, water-, oil-,

https://doi.org/10.1021/acsami.5c20801
ACS Appl. Mater. Interfaces 2026, 18, 3262−3273

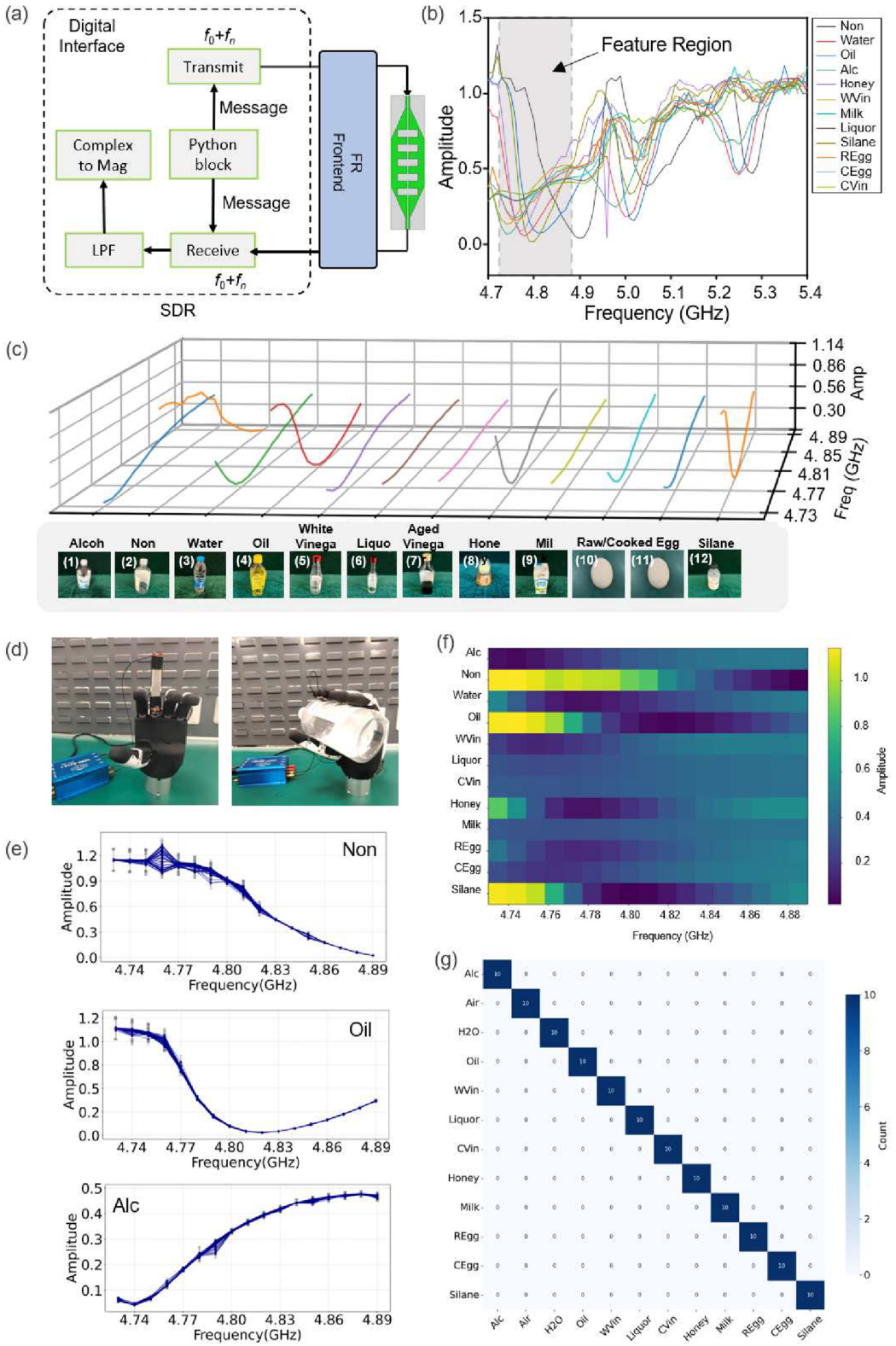

Figure 5. Material identification capability of the SSPP flexible sensor. (a) System schematic for material identification. (b) Frequency-sweeping characteristics of the SSPP sensor under various materials. (c) 3D plots of the SSPP sensor outputs corresponding to different objects. (d) Integration of sensors with dexterous hands. (e) Forty-trial output characteristics and test images for objects. (f) Rate-amplitude heatmap of 12 states. (g) The confusion map for the machine learning (KNN) outcome of 12 objects.

alcohol-, honey-, and white wine: WVin, milk, liquor, silane, raw egg: REgg, cooked egg: CEgg, vinegar: CVin) over the frequency range of 4.7−5.4 GHz. The results show that the differences in dielectric properties and loss factors lead to distinct amplitude spectral features within the characteristic region (feature region, highlighted in gray) acquired from the corresponding material. High-permittivity and high-loss materials (e.g., water and milk) cause significant resonance

https://doi.org/10.1021/acsami.5c20801
ACS Appl. Mater. Interfaces 2026, 18, 3262−3273

Table 2. Dielectric Properties of the Samples

sample	dielectric constant ε' (5 GHz)	loss tangent tan δ (5 GHz)
air	~1	~0
water[53]	~70−75	~0.25
alcohol[52]	~4.5−5	~0.71
liquor (42%)[53]	~40	~0.625
oil[56]	~2.2−3.5	<0.01
aged vinegar (4%)[54]	~68	~0.33
honey[55]	~13−20	~0.4−0.5
milk[57]	~58−60	~0.33
raw egg[58]	~50−55	~0.2
cooked egg[59]	~35−45	~0.4−0.5
white vinegar (8%)[54]	~65	~0.35

peak broadening and strong amplitude attenuation, whereas low-loss substances (e.g., oil, silane) show narrower resonance peaks and higher amplitude. The gray feature region (approximately 4.73−4.89 GHz) is selected as the optimized operating band, as it covers the characteristic resonance points of most materials and maximizes amplitude differentiation. Restricting the frequency-sweep range significantly improves system response speed without compromising classification accuracy. These results validate the feasibility of rapid material identification based on narrowband frequency sweeping and provide a design basis for real-time penetrable sensing applications.

Furthermore, the swept-frequency experiments were conducted within the characteristic frequency region (4.73−4.89 GHz). The data in Figure 5c compare the amplitude responses of 12 different materials and illustrate the spectral variation across the tested materials. Each material corresponds to an individual spectral curve, with vertical offsets clearly illustrating amplitude differences: high-loss dielectrics (such as water and milk) exhibit significant amplitude attenuation near the resonant frequency (amplitude below 0.3), while low-loss dielectrics (e.g., air (Non), oil, and silane) maintain relatively high amplitude responses (above 0.8). Noticeably, raw and cooked eggs (Raw/Cooked Egg) show distinguishable spectral shifts due to dielectric property variations caused by protein denaturation. Meanwhile, alcoholic substances (alcohol, liquor) and vinegar types (white vinegar, aged vinegar) are clearly separated in the spectral domain owing to differences in composition and concentration. The above results validate the sensitivity of the characteristic frequency region (highlighted in gray in Figure 5b) to the dielectric properties of the materials. Furthermore, the two-dimensional mapping between amplitude and frequency provides a discriminative feature space enabling penetrable multimaterials classification. The integration effect of the flexible SSPP sensor with a dexterous hand is shown in Figure 5d. The sensor can be observed to conformally adhere to the finger joints and the fingertip region (middle finger), with the TPU substrate and conductive silver paste exhibiting sufficient flexibility to accommodate the motion of the finger joints. The right panel of Figure 5d shows a photograph of the sensor-equipped dexterous hand grasping a bottle.

To prove the signal stability and consistency of the as-fabricated SSPP, the cyclic experiments were conducted within the optimized characteristic frequency region (4.73−4.89 GHz). Each of the four representative materials, including empty: non, vinegar: CVin, oil: Oil, alcohol: Alc, was tested by 40 repeated measurements (Figures 5e and S5). All 40 curves for each sample exhibit high consistency: the curves of empty bottle(Non) are concentrated in the high-amplitude range (0.9−1.2 when f_{RF} = 4.73−4.8 GHz) with smooth spectral profiles and no distortion; vinegar (CVin) shows significant amplitude attenuation (0.30−0.43) due to its high dielectric constant, and its data curves form a tightly grouped distribution (Figure S5); oil, as a low-loss medium, maintains the highest amplitude response with a sharp resonance peak; alcohol (Alc) curves are distributed in the intermediate amplitude range (0.1−0.5). These results demonstrate the excellent repeatability and stability of the SSPP sensor within the characteristic frequency region. Significant amplitude differences are observed among the different materials. Moreover, the standard deviation of curves within the same material is less than 0.05, indicating that the system can achieve highly reliable material identification based on narrowband frequency sweeping, thereby ensuring data robustness for classification algorithms in practical applications.

The frequency-amplitude heatmap visually illustrates the electromagnetic response distribution of 12 substances across the characteristic frequency band of 4.73−4.89 GHz (Figure 5f), where the color depth represents the normalized amplitude intensity (range: 0.2−1.0). A strong correlation was observed between the amplitude response and the dielectric properties of the substances: low-loss dielectrics (air, oil, silane) exhibit high-intensity warm-colored regions (amplitude >0.8) near the resonant frequency, while high-loss dielectrics (water, milk, honey) display low-intensity cool-colored regions (amplitude <0.4). Notably, Raw and cooked eggs exhibit distinguishable amplitude gradients in the heatmap, resulting from differences in protein state. The heatmap effectively reveals the clustering behavior of characteristic spectra across substances for machine learning-based classification.

Figure 5g presents the confusion matrix of the machine learning-based classification results for the 12 substances (Figure S6). The results demonstrate perfect classification accuracy: all diagonal elements show a value of 12 (indicating that all 12 test samples of each substance were correctly identified), while all off-diagonal elements are zero (implying no misclassification). This indicates that the machine learning model, trained using features extracted from the SSPP sensor's frequency-swept responses, achieved 100% classification accuracy. These results fully validate the high discriminative power of the parameters, such as amplitude and spectral morphology, extracted within the characteristic frequency region. This outcome demonstrates the high reliability and practical utility of the proposed sensing system combined with machine learning algorithms in the field of substance identification.

3. CONCLUSIONS

Current robotic manipulators with various types of tactile sensors offer the possibility of human-like dexterous operation via the detection of different physical stimuli. However, the requirement of high compatibility in various applications raises the need to make robots with advanced perception capabilities. Multimodal and cross-media penetrable sensing functions are necessary to ensure a comprehensive understanding of the operated object with enough precaution. In this study, a flexible e-skin-based SSPP sensor is designed and fabricated by screen-printing conductive silver paste onto a 0.6-mm-thick

https://doi.org/10.1021/acsami.5c20801
ACS Appl. Mater. Interfaces 2026, 18, 3262−3273

TPU substrate to form a periodic gradient-grooved structure. Operating in the 4.7−5.4 GHz frequency band, the sensor demonstrates dual functionality for both proximity/contact sensing and penetrable material identification. It achieves millimeter-level proximity detection by monitoring phase variations as an object approaches, while reliable material identification within containers is accomplished through spectral changes upon contact. Within the characteristic frequency band of 4.73−4.89 GHz, the sensor demonstrates significant spectral response distinctions across 12 typical materials, with amplitude and phase variations strongly correlated to the dielectric constant and loss tangent of the materials. By optimizing a narrowband frequency-sweeping strategy, the system significantly improves the detection efficiency while maintaining feature discriminability. A machine learning classification model achieved 100% accuracy, and 40 repeated measurements showed highly consistent curves, confirming the excellent reproducibility and stability of the system. Mechanical deformation tests confirm that the sensor maintains a stable electromagnetic performance, with a frequency drift of less than 3%, even under bending and twisting conditions up to 80°.

The proposed flexible sensor with the corresponding sensing approach offers a novel method that has potential in scenarios requiring simultaneous physical perception and chemical identification under complex operations. Hence, its cross-media sensing capability with low cost and compact and flexible features can benefit industrial inspection, biomedical development, healthcare, daily assistance, etc.

4. METHODS

4.1. SSPP Sensor Design

The SSPP sensor was designed with specific geometric parameters to support SSPP modes exhibiting the desired wavenumber across the 4.7−5.4 GHz frequency band. The dispersion relation of the metamaterial structure, which governs the wavenumber β, is given by

$$\beta = k_0\sqrt{\varepsilon_1\varepsilon_2/(\varepsilon_1 + \varepsilon_2)} \tag{1}$$

where $k_0 = \omega/c$ is the wavenumber, ε_1 is the dielectric permittivity and $\varepsilon_2 = 1 - \omega_p^2/\omega^2$. The dispersion curve lies to the right of the light line ($\beta = k_0$) and approaches a horizontal asymptote at the surface plasma frequency $\omega_{sp} = \omega_p/\sqrt{1 + \varepsilon_1}$. The transmission efficiency of the linearly tapered matching section was evaluated through $|S_{11}|$ simulations, which confirmed efficient wavevector conversion by the proposed structure. The conductive silver paste, a TPU-based stretchable formulation, exhibits high flexibility and can be cured at a low temperature of 90 °C. A FPC board with a thickness of 0.12 mm was employed to connect the microstrip line, composed of the silver paste, to an IPEX4 connector.

4.2. Fabrication Process of the Proposed Flexible SSPP

As illustrated in Figure 1e, the periodic SSPP conductive structure, tapered transition, and microstrip line were screen-printed onto a TPU substrate using stretchable silver paste (LY-508) with low-temperature curing capability, serving as the core sensing unit. This material choice ensures high electrical conductivity and mechanical compliance under deformation. The printed structure was then subjected to an initial thermal curing step at 80 °C to stabilize the conductive pattern and enhance interfacial adhesion. Subsequently, the substrate was flipped and aligned, followed by screen-printing a shielding layer on the backside to mitigate external interference. A second thermal curing process was applied to ensure the structural integrity of the shielding layer and robust interlayer adhesion. The cured SSPP structure was then laser-cut or die-cut into individual sensor units. Following this, an IPEX4 RF connector was aligned and soldered onto the FPC layer. The separated SSPP element was positioned on a workstage, and the FPC layer was integrated onto both microstrip line sections to establish electrical interconnection and mechanical support between the IPEX interface and the SSPP structure. The connection between the FPC and the printed structure was realized using anisotropic conductive tape, which conducts only in the direction normal to the circuit surface. Finally, a coaxial cable was assembled to the IPEX connector to complete the high-frequency signal transmission interface. The entire process employs multistep printing and low-temperature curing strategies, enabling high-precision integration of functional layers while preserving the mechanical properties of the flexible substrate. The SSPP periodic structure consists of rectangular grooves with a period of p, a depth of h, and a TPU layer thickness of t.

4.3. System Setup

The system components were interconnected with a software-defined radio (SDR, B210 USRP) using coaxial cables. The radio was programmed to transmit and receive continuous-wave signals at a carrier frequency of f_{RF} = 4.7−5.4 GHz, upconverted from a baseband signal at f_0 = 1 kHz sampled at 32 kHz. These signals were conformally guided along the sensor, where they interacted with external substances, capturing the spectral changes mixed into the returned RF signal (Figure 4a). In the proximity/contact sensing system, the carrier frequency is 5 GHz, the fundamental signal is 1 kHz, and the sampling frequency is 10 kHz. The principle for detecting the proximity of objects in this study is based on radar ranging utilizing the Doppler effect. The instantaneous phase of the received signal is

$$\phi(t) = 2\pi f\frac{2R(t)}{c} + \phi_0 \tag{2}$$

where $R(t)$ represents the instantaneous distance between the target and the radar/sensor, c is the speed of light, and ϕ_0 denotes the initial phase (a constant). Digital complex Doppler signals were generated through conjugate multiplication of the baseband transmitted signal and the down-converted received signal. Subsequently, phase variations were extracted from the complex Doppler signals via arctangent demodulation, followed by phase unwrapping. In the material identification system, synchronization of carrier frequency switching between transmission and reception was achieved by using a message-based control module. In this work, 80,960 data points are acquired per frequency band across a total of 18 frequency points, with a sampling rate of 32 kHz, resulting in a total frequency-sweeping time of 45 s. The acquired data from various substances were processed using a k-Nearest Neighbors (KNN) machine learning algorithm implemented in Python. The training data set consists of 40 groups per material, with 10 groups reserved for validation. A KNN algorithm is employed, and the extracted features include: time-domain features (reflecting overall response strength and stability) such as the mean, standard deviation, and peak-to-peak value of the frequency-swept curve; frequency-domain features including the normalized dominant frequency position, the strength of the highest-frequency component, and the lowest-frequency component; morphological features such as the number of rising points; and key-frequency-point features. Leave-One-Out cross-validation (LOO) was performed, yielding an array of cross-validation accuracy scores.

4.4. Numerical Simulation

Electromagnetic simulations were performed using HFSS. The dispersion curves of the SSPP structure were obtained with the eigenmode solver, in which the unit cell was defined with periodic boundary conditions. Field distributions were calculated by using the full sensor structure excited by a wave port. To evaluate phase variations, a cylindrical equivalent model representing an ethanol solution ($\varepsilon_r = 4.5 + 2i$) was positioned above the SSPP structure. Parametric sweeping was applied to the model to simulate spatial changes in the dielectric properties induced by proximity and contact events. The resulting phase changes were extracted from the S_{21} parameter in the simulations.

https://doi.org/10.1021/acsami.5c20801
ACS Appl. Mater. Interfaces 2026, 18, 3262−3273

■ ASSOCIATED CONTENT

Data Availability Statement

All data needed to evaluate the conclusions in the paper are present in the paper and/or the Supporting Information.

Supporting Information

The Supporting Information is available free of charge at https://pubs.acs.org/doi/10.1021/acsami.5c20801.

Details of a Flexible SSPP sensing system based on software-defined radio (Figure S1); measurement method for sensor bending and torsion angles (Figure S2); test setup for the mechanical cycling characteristics of the sensor (Figure S3); cycling test results (Figure S4); forty sets of frequency-sweep data (Figure S5); schematic diagram of KNN method (Figure S6) (PDF)

■ AUTHOR INFORMATION

Corresponding Authors

Chengkuo Lee − *Department of Electrical & Computer Engineering, National University of Singapore, Singapore 117576, Singapore;* orcid.org/0000-0002-8886-3649; Email: elelc@nus.edu.sg

Minglu Zhu − *School of Mechanical and Electrical Engineering, Soochow University, Suzhou, Jiangsu 215137, China;* orcid.org/0000-0001-6652-2133; Email: mlzhu@suda.edu.cn

Tao Chen − *School of Future Science and Engineering, Soochow University, Suzhou, Jiangsu 215222, China;* Email: chent@suda.edu.cn

Authors

Yongze Li − *School of Future Science and Engineering, Soochow University, Suzhou, Jiangsu 215222, China;* orcid.org/0000-0002-5431-3921

Shuhao Zhang − *School of Future Science and Engineering, Soochow University, Suzhou, Jiangsu 215222, China*

Xuan Li − *School of Mechanical and Electrical Engineering, Soochow University, Suzhou, Jiangsu 215137, China*

Complete contact information is available at: https://pubs.acs.org/10.1021/acsami.5c20801

Author Contributions

Conceptualization: Y.L.; methodology: C.L. and X.L.; investigation: S.Z. and M.Z.; writing-original draft: Y.L.; writing-review and editing: M.Z. and T.C.

Funding

This work was funded by the National Natural Science Foundation of China (Grant numbers 62573309 and 62303340) and the Natural Science Foundation of Jiangsu Province of China (Grant number BK20230480).

Notes

The authors declare no competing financial interest.

■ REFERENCES

(1) Chen, R.; Zhang, H.; Zhou, S.; Xu, X.; Yuan, Z.; Wang, H.; Luo, J. A Rigid-Flexible-Soft Coupled Dexterous Hand With Sliding Tactile Perception and Feedback. *IEEE Robot. Autom. Lett.* **2024**, *9*, 1158−1163.

(2) Huang, J.; Chen, K.; Zhou, J.; Lin, X.; Abbeel, P.; Dou, Q.; Liu, Y. Dexterous In-Hand Teleoperation Framework for Learning Multiobjects Manipulation With Tactile Sensing. *IEEE/ASME Trans. Mechatron.* **2025**, *1*, 3840−3851.

(3) Zhang, B.-B.; Zhang, D.; Li, Y.; Lu, Z.; Chen, J.; Wang, H.; Zhou, F.; Pu, Y.; Hu, Y.; Ma, L.-K.; Sun, Q.; Chen, Y. Monitoring Long-Term Cardiac Activity with Contactless Radio Frequency signals. *Nat. Commun.* **2024**, *15*, 10598.

(4) Zhang, Z.; Sharma, P.; Zhou, J.; Hui, X.; Kan, E. C. Furniture-Integrated Respiration Sensors by Notched Transmission Lines. *IEEE Sens. J.* **2021**, *21*, 5303.

(5) Zhao, C.; Xie, L.; Huang, B.; Wang, S.; Ma, D. Tactile-Driven Dexterous In-Hand Writing via Extrinsic Contact Sensing. *IEEE Robot. Autom. Lett.* **2025**, *10*, 8914.

(6) Loutchanwoot, P.; Harnsoongnoen, S. Microwave Microfluidic Sensor for Detection of High Equol Concentrations in Aqueous Solution. *IEEE Trans. Biomed. Circuits Syst.* **2022**, *16*, 244.

(7) Ye, W.; Wang, D.-W.; Wang, J.; Chen, S.; Wang, G.; Zhao, W.-S. An Ultrahigh-Sensitivity Dual-Mode Microwave Sensor for Microfluidic Applications. *IEEE Microw. Wireless Technol. Lett.* **2023**, *33*, 1082.

(8) Park, J.; Jung, D.; Lee, Y.; Park, D.; Choi, J.; Kim, U. Tactile Sensor Integrated Fingertip Capable of Detecting Precise Contact Force for Robotic Grippers. *IEEE Trans. Ind. Electron.* **2025**, *72*, 5105.

(9) Hu, Y.; Bai, H.; Deng, R.; Yang, W. ECT Sensor for Symmetrical Robot Gripper Application. *IEEE Trans. Instrum. Meas.* **2025**, *74*, 1.

(10) Sun, J.; Zhang, D.; Zhang, R.; Zhang, J.; Zhao, Q.; He, H.; Huang, H.; Yang, L.; Xu, Y. Novel Polyurethane Based, Fully Flexible, High-Performance Piezoresistive Sensor for Real-Time Pressure Monitoring. *ACS Appl. Mater. Interfaces.* **2024**, *16*, 25422.

(11) Chen, Z.; Qu, C.; Yao, J.; Zhang, Y.; Xu, Y. Two-Stage Micropyramids Enhanced Flexible Piezoresistive Sensor for Health Monitoring and Human-Computer Interaction. *ACS Appl. Mater. Interfaces.* **2024**, *16*, 7640.

(12) Zhao, H.; Chen, X.; Xin, C.; Zhao, F.; Cheng, S.; Lei, M.; Wang, C.; Zhang, J.; Chen, X.; Tian, H.; Zhang, J.; Shao, J. High-sensitivity and Self-Powered Flexible Pressure Sensor Based on Multi-scale Structured Piezoelectric Composite. *Chem. Eng. J.* **2025**, *519*, No. 164787.

(13) Wu, G.; Li, X.; Bao, R.; Pan, C. Innovations in Tactile Sensing: Microstructural Designs for Superior Flexible Sensor Performance. *Adv. Funct. Mater.* **2024**, *34*, No. 2405722.

(14) Li, Z.; Zhao, K.; Wang, J.; Wang, B.; Lu, J.; Jia, B.; Ji, T.; Han, X.; Luo, G.; Yu, Y.; Wang, L.; Li, M.; Wang, Z.; Zhao, L. Sensitive, Robust, Wide-Range, and High-Consistency Capacitive Tactile Sensors with Ordered Porous Dielectric Microstructures. *ACS Appl. Mater. Interfaces.* **2024**, *16*, 7384.

(15) Chen, C.-Y.; Kuo, C.-T.; Hu, L.-H. Highly Transparent and Stretchable Multi-layered Capacitive Film Sensor with Flexible Dot and Micro-Pillar Array for Small Pressure Sensing. *Sens. Actuators A Phys.* **2024**, *376*, No. 115605.

(16) Huang, X.; Ma, Z.; Xia, W.; Hao, L.; Wu, Y.; Lu, S.; Luo, Y.; Qin, L.; Dong, G. A High-Sensitivity Flexible Piezoelectric Tactile Sensor Utilizing an Innovative Rigid-in-Soft Structure. *Nano Energy.* **2024**, *129*, No. 110019.

(17) Park, H.; Gbadam, G. S.; Niu, S.; Ryu, H.; Lee, J.-H. Manufacturing Strategies for Highly Sensitive and Self-Powered Piezoelectric and Triboelectric Tactile Sensors. *Int. J. Extrem. Manuf.* **2025**, *7*, 12006.

(18) Hashem, R.; El-Hussieny, H.; Umezu, S.; El-Bab, A. M. R. F. Integrating Finite Element Analysis and Machine Learning for Non-Invasive Tumor Detection: a Piezoelectric Tactile Sensor-based Vibration Absorber Approach. *Neural Comput. Applic.* **2025**, *37*, 12059.

(19) Peng, W.; Zhu, R.; Ni, Q.; Zhao, J.; Zhu, X.; Mei, Q.; Zhang, C.; Liao, L. Functional Tactile Sensor Based on Arrayed Triboelectric Nanogenerators. *Adv. Energy Mater.* **2024**, *14*, No. 2403289.

(20) Liu, Y.; Wang, J.; Liu, T.; Wei, Z.; Luo, B.; Chi, M.; Zhang, S.; Cai, C.; Gao, C.; Zhao, T.; Wang, S.; Nie, S. Triboelectric Tactile Sensor for Pressure and Temperature Sensing in High-temperature Applications. *Nat. Commun.* **2025**, *16*, 383.

(21) Lee, E.-I.; Ko, H.-J.; Kim, J.; Park, J.-W. Self-Powered Single Multifunctional Tactile Sensor for Simultaneous Detection of Dynamic and Static Pressure and Temperature Inspired by Skin Sensory Functions. *Nano Energy.* **2025**, *139*, No. 110984.
(22) Liu, M.; Dai, Z.; Zhao, Y.; Ling, H.; Sun, L.; Lee, C.; Zhu, M.; Chen, T. Tactile Sensing and Rendering Patch with Dynamic and Static Sensing and Haptic Feedback for Immersive Communication. *ACS Appl. Mater. Interfaces.* **2024**, *16*, 53207−53219.
(23) Fang, P.; Zhu, M.; Zeng, Z.; Lu, W.; Wang, F. X.; Zhang, L.; Chen, T.; Sun, L. A Multi-Module Sensing and Bi-Directional HMI Integrating Interaction, Recognition, and Feedback for Intelligent Robots. *Adv. Funct. Mater.* **2024**, *34*, No. 2310254.
(24) Chen, T.; Dai, Z.; Liu, M.; Zhao, Y.; Ling, H.; Sun, L.; He, H.; Lee, C.; Zhu, M. 3D Multimodal Sensing and Feedback Finger Case for Immersive Dual-Way Interaction. *Adv. Mater. Technol.* **2024**, *9*, No. 2301681.
(25) Yu, Y.; Jain, B.; Anand, G.; Heidarian, M.; Lowe, A.; Kalra, A. Technologies for Non-Invasive Physiological Sensing: Status, Challenges, and Future Horizons. *Biosens. Bioelectron. X.* **2024**, *16*, No. 100420.
(26) Yao, N.; Wang, S. Recent Progress of Optical Tactile Sensors: A Review. *Opt. Laser Technol.* **2024**, *176*, No. 111040.
(27) Son, C.; Kim, J.; Kang, D.; Park, S.; Ryu, C.; Baek, D.; Jeong, G.; Jeong, S.; Ahn, S.; Lim, C.; Jeong, Y.; Eom, J.; Park, J.-H.; Lee, D. W.; Kim, D.; Kim, J.; Ko, H.; Lee, J. Behavioral Biometric Optical Tactile Sensor for Instantaneous Decoupling of Dynamic Touch Signals in Real Time. *Nat. Commun.* **2024**, *15*, 8003.
(28) Li, H.; Nam, S.; Lu, Z.; Yang, C.; Psomopoulou, E.; Lepora, N. F. BioTacTip: A Soft Biomimetic Optical Tactile Sensor for Efficient 3D Contact Localization and 3D Force Estimation. *IEEE Robot. Autom. Lett.* **2024**, *9*, 5314.
(29) Hui, X.; Kan, E. C. No-touch Measurements of Vital Signs in Small Conscious Animals. *Sci. Adv.* **2019**, *5*, No. eaau0169.
(30) Banerjee, A.; Kumar, A.; Tiwari, N. K.; Akhtar, M. J. Design of Bridge Type C-Band Planar RF Sensor for Detection of Solute Concentration Level in Water. *IEEE Sens. J.* **2021**, *21*, 22670.
(31) Yang, X.; Zhang, M.; Ren, M.; Mao, S.; Dhakal, R.; Kim, N.-Y.; Cao, Y.; Li, Y.; Yao, Z. Ultra-fast and High-Sensitive Tacrolimus Solution Detection Based on Microwave Biosensor. *Sens. Actuators A Phys.* **2023**, *354*, No. 114282.
(32) Wu, W.-J.; Zhao, W.-S.; Wang, W. A Novel Microwave Sensor Based on Modified Rat-Race Coupler for Extracting Real Permittivity and Concentration of Binary Aqueous Solution. *IEEE Sens. J.* **2024**, *24*, 14213.
(33) Luo, W.; Li, C.; Wang, L.; Qian, L.; Li, D.; Miao, L.; Xiong, Y.; Li, M.; Tian, Y.; Li, H. Microwave Humidity Sensor Based on Shorted Split Ring Resonator with Interdigital Capacitance and α-Al2O3 Nanoflakes/Chitosan Sensitive Film for Respiration Monitoring. *Sens. Actuators B Chem.* **2024**, *413*, No. 135869.
(34) Li, C.; Lubecke, V. M.; Boric-Lubecke, O.; Lin, J. A Review on Recent Advances in Doppler Radar Sensors for Noncontact Healthcare Monitoring. *IEEE Trans. Microw. Theory Techn.* **2013**, *61*, 2046.
(35) Wu, J.-K.; Yue, W.; Gao, K.; von Gratowski, S.; Gu, X.-F.; Pan, L.; Kim, N.-Y.; Liang, J.-G. Microwave-Sensor Array for Decoupling Detection of Distance, Shape, Dielectric, and Morphology. *IEEE Trans. Instrum. Meas.* **2023**, *72*, 1.
(36) Zhu, C.; Alsalman, O.; Huang, J. Accurate, and Noncontact Material Identification Using a Single Microwave Sensor With Machine Learning Analysis. *IEEE Trans. Instrum. Meas.* **2024**, *73*, 1.
(37) Shrivastav, A. M.; Cvelbar, U.; Abdulhalim, I. A comprehensive review on plasmonic-based biosensors used in viral diagnostics. *Commun. Biol.* **2021**, *4*, 70.
(38) Ahmadivand, A.; Gerislioglu, B.; Ahuja, R.; Mishra, Y. K. Terahertz plasmonics: The rise of toroidal metadevices towards immunobiosensings. *Mater. Today* **2020**, *32*, 108−130.
(39) Podunavac, I.; Radonic, V.; Bengin, V.; Jankovic, N. Microwave Spoof Surface Plasmon Polariton-Based Sensor for Ultrasensitive Detection of Liquid Analyte Dielectric Constant. *Sensors.* **2021**, *21*, 5477.
(40) Ye, L.; Xiao, Y.; Liu, Y.; Zhang, L.; Cai, G.; Liu, Q. H. Strongly Confined Spoof Surface Plasmon Polaritons Waveguiding Enabled by Planar Staggered Plasmonic Waveguides. *Sci. Rep.* **2016**, *6*, 38528.
(41) Liu, Y.; Fang, C.; Han, G.; Shao, Y.; Huang, Y.; Wang, H.; Wang, Y.; Zhang, C.; Hao, Y. Ultrathin Corrugated Metallic Strips for Ultrawideband Surface Wave Trapping at Terahertz Frequencies. *IEEE Photonics J.* **2017**, *9*, 1.
(42) Kianinejad, A.; Chen, Z. N.; Qiu, C.-W. A Single-Layered Spoof-Plasmon-Mode Leaky Wave Antenna With Consistent Gain. *IEEE Trans. Antennas Propag.* **2017**, *65*, 681.
(43) Han, X.; Li, X.; Zhou, Y.; Ma, Z.; Peng, P.; Fu, C.; Qiao, L. Microwave Sensor Loaded With Complementary Curved Ring Resonator for Material Permittivity Detection. *IEEE Sens. J.* **2022**, *22*, 20456.
(44) Zhang, X.; Zhu, J. W.; Cui, T. J. An Ultracompact Spoof Surface Plasmon Sensing System for Adaptive and Accurate Detection of Gas Using a Smartphone. *Engineering* **2024**, *35*, 86.
(45) Zeng, Q.; Tian, X.; Nguyen, D. T.; Li, C.; Chia, P.; Tee, B. C. K.; Wu, C.; Ho, J. S. A Digitally Embroidered Metamaterial Biosensor for Kinetic Environments. *Nat. Electron.* **2024**, *7*, 1025.
(46) Nguyen, D. T.; Zeng, Q.; Tian, X.; Ho, J. S. Ambient Health Sensing on Passive Surfaces Using Metamaterials. *Sci. Adv.* **2024**, *10*, No. eadj6613.
(47) Tian, X.; Lee, P. M.; Tan, Y. J.; Wu, T. L. Y.; Yao, H.; Zhang, M.; Li, Z.; Ng, K. A.; Tee, B. C. K.; Ho, J. S. Wireless Body Sensor Networks Based on Metamaterial Textiles. *Nat. Electron.* **2019**, *2*, 243.
(48) Chen, Z.; Lin, W.; Zhang, C.; et al. Multifunctional and reconfigurable electronic fabrics assisted by artificial intelligence for human augmentation. *Advanced Fiber Materials* **2024**, *6* (1), 229−242.
(49) Lin, W.; Xu, Y.; Yu, S.; et al. Highly programmable haptic decoding and self-adaptive spatiotemporal feedback toward embodied intelligence. *Adv. Funct. Mater.* **2025**, *35* (38), No. 2500633.
(50) Lin, W.; Wang, H.; Wangyuan, R.; et al. Dielectrically modified polymer and topologically optimized microstructure enabling in-sensor decoupling for multifunctional human−machine interactions. *Adv. Funct. Mater.* **2025**, *35* (44), No. 2505912.
(51) Shen, X.; Cui, T. J.; Martin-Cano, D.; Garcia-Vidal, F. J. Conformal surface plasmons propagating on ultrathin and flexible films. *Proceedings of the National Academy of Sciences of the United States of America.* **2013**, *110* (1), 40−45.
(52) Gregory, A. P.; Clarke, R. N. *Tables of the Complex Permittivity of Dielectric Reference Liquids at Frequencies up to 5 GHz*; National Physical Laboratory: Teddington, UK, 2012.
(53) Bohigas, X.; Tejada, J. Dielectric characterization of alcoholic beverages and solutions of ethanol in water under microwave radiation in the 1−20 GHz range. *Food Research International.* **2010**, *43* (6), 1607−1613.
(54) Bohigas, X.; Tejada, J. Dielectric properties of acetic acid and vinegar in the microwave frequencies range 1−20 GHz. *Journal of Food Engineering.* **2009**, *94* (1), 46−51.
(55) Cheng, E. M.; Lee, K. Y.; Khor, S. F.; et al. Microwave dielectric and reflection analysis on pure and adulterated Trigona honey and honey gold. *Radioengineering.* **2022**, *31* (3), 281−294.
(56) Lu, Q.-Q.; Cheng, Y.-D.; Jin, Y.-Z. Correlation research between dielectric constant and the quality variation for vegetable oil. *Sci. Technol. Food Ind.* **2015**, *7*, 109−112.
(57) Liu, Q.; Guo, W.; Zhu, X. Effect of lactose content on dielectric properties of whole milk and skim milk. *International Journal of Food Science and Technology.* **2018**, *53* (9), 2037−2044.
(58) Miura, N.; Yagihara, S.; Mashimo, S. Microwave dielectric properties of solid and liquid foods investigated by time-domain reflectometry. *Journal of Food Science.* **2003**, *68* (4), 1396−1403.
(59) Jain, R. C.; Voss, W. A. G. Dielectric properties of raw and cooked chicken egg at 3 GHz, 23 — 140°C. *Journal of Microwave Power and Electromagnetic Energy.* **1987**, *22* (4), 221−227.

https://doi.org/10.1021/acsami.5c20801
ACS Appl. Mater. Interfaces 2026, 18, 3262−3273